International Journal of Modern Physics E
Vol. 27, No. 2 (2018) 1850012 (21 pages)

DOI: 10.1142/S021830131850012X

Decay properties and reaction dynamics of zirconium isotopes in the relativistic mean-field model

M. Panigrahi and R. N. Panda*

Department of Physics,
Siksha 'O' Anusandhan, Deemed to be University,
Bhubaneswar 751030, Odisha, India
**rabipandababu@rediffmail.com*

Bharat Kumar and S. K. Patra

Institute of Physics, Sachivalaya Marg,
Bhubaneswar 751005, Odisha, India

Homi Bhabha National Institute, Anushakti Nagar,
Mumbai 400085, Maharashtra, India

Received 10 July 2017
Revised 17 January 2018
Accepted 18 January 2018
Published 20 February 2018

In the framework of relativistic mean-field theory, the ground state properties like binding energy, charge radius and quadrupole deformation parameter for various isotopes of zirconium from the valley of stability to drip-line region have been studied. The results are compared with the experimental data and we found reasonable agreement. The calculations are carried out for β-decay energy and β-decay half-life up to the drip-line. Total reaction and elastic differential cross-sections are also studied for few zirconium isotopes as projectiles with ^{12}C as target, using different parameter sets namely NL3*, DD-ME2 and DD-PC1 in conjunction with Glauber model.

Keywords: Relativistic mean-field theory; matter density distribution; Glauber theory; decay modes; total nuclear reaction cross-section.

PACS Number(s): 21.10.Dr, 21.10.Ft, 23.40.−s, 25.60.Dz

1. Introduction

The study of heavy unstable nuclei near the drip-line region of nuclear chart has opened a new area of research in the nuclear structure physics for finite systems.[1–4] This study is not only an interesting topic in nuclear structure physics but also provides information about the synthesis of new elements due to stellar evolution.[5–7] The structural properties of nuclei far away from the β-stability line are also active

*Corresponding author.

areas of research in both theories and experiments.[8–10] In particular, the neutron-rich Zr, Mo, Ru and Pd with mass number A in the range of 100–130 are of special interest for various reasons, i.e., they lie far away from the β-stable region of *nuclear landscape*, thus resulting in well-established deformation.[9,11,12] Moreover, one can expect to see several new phenomena as follows: much diffused neutron matter distribution gives rise to the "neutron skin" and "neutron halos".[13] In a recent study Meng and Zhou[14] have explained the phenomena of giant halos consisting of up to six halo neutrons close to the neutron drip line in Zr isotopes. Nomura *et al.*[15] also showed the rapid structural change between $N = 58$ and $N = 60$ in $^{94-110}$Zr, within the SCMF-to-IBM mapping procedure based on the Gogny-D1M EDF. Some other authors[16,17] have also analyzed many basic properties of Zr isotopes. Further, new collective modes associated with the neutron skin, e.g., "scissors" vibrational mode, are predicted in Ref. 18. The study of β-decay and β-delayed particle emission of exotic nuclei enhances our understanding of the nature of different interactions. Moreover, β-decay property also help to understand the isotopic abundance and the possible r-process paths. Zirconium is an important and major component of the structural materials used in traditional and advanced nuclear reactions, owing to its very low absorption cross-sections for thermal neutrons and resistance to corrosion.[19] Moreover zirconium is intended to be used in the blanket and first wall of fusion reactors because of its high temperature durability. About 90% of zirconium produced is frequently used for cladding of fuel rods, in calandria vessel and pipelines of secondary coolant circuit in nuclear reactors in the form of zircaloy. In addition to its use in current nuclear reactors, zirconium is present in most of the innovative concepts.[20] This indicates that the cross-section data are required in a broad energy range for better understanding of the properties of Zr. In the recent few decades, the nuclear physicists are much more interested in $A = 100$ mass region, due to various coexisting nuclear shapes (well deformed, prolate, oblate and spherical).[21] Here, we have considered the zirconium isotopic chain from proton-rich ^{90}Zr to the drip-line nuclei, which comes under this $A = 100$ mass region.

In this present work we have investigated the bulk structural properties like binding energy (BE), root-mean-square (RMS) charge radius ($r_{\rm ch}$), neutron and proton radii (r_n and r_p), quadrupole deformation parameter (β_2), one-neutron and one-proton separation energies (S_n and S_p). We have also studied the β-decay properties of Zr isotopes up to the expected drip-line nuclei at mass number $A = 125$. Reaction dynamics like total nuclear reaction (σ_R) and angular elastic differential cross-sections ($d\sigma/d\Omega$) have been studied at 800 MeV/A, for few isotopes of zirconium in the framework of Glauber formalism.[22,23] Here the zirconium isotopes are taken as projectiles reacting with carbon (^{12}C) as the target. We have calculated the cross-sections by using both spherical and deformed densities from the well-known relativistic mean-field (RMF) model with NL3*, DD-ME2 and DD-PC1 parameter sets.

The paper is organized as follows: The RMF formalism, β-decay half-life and the reaction mechanism in the framework of Glauber model are explained briefly in Sec. 2. The results obtained from our calculations are discussed in Sec. 3. This section also includes the results for β-decay energy (Q_β) and β-decay half-lives ($T_\beta^{1/2}$) for the zirconium isotopic chain. Finally, the main conclusions of this work are summarized in Sec. 4.

2. Theoretical Formalism

To get a precise knowledge and understanding about nuclear reaction systematics along with the nuclear structure, several theoretical models have been a matter of wide interest. In this juncture, the RMF model provides the internal structure or substructure information of the nuclei through density distributions,[24] as it considers the nuclei as a composite system of nucleons (protons and neutrons) interacting by means of the exchange of mesons and photons.[25–32] The use of RMF formalism for finite nuclei as well as infinite nuclear matter is well documented and details can be found in Refs. 30–34 and Refs. 35–38, respectively. The working expressions for the density profile and other terminologies could be found in Refs. 30–32 and 35–42. Three classes of covariant energy density functional (CEDF) models are used in this paper, i.e., the nonlinear meson–nucleon-coupling models (NL), the density-dependent meson-exchange (DD-ME) models and the density-dependent point-coupling (DD-PC) models. The remarkable difference between them is in their density dependence and the interaction range. In NL and DD-ME models, the interaction has a finite range which is estimated from the mass of the mesons. For realistic calculations the density dependence is very important, which is taken into account by nonlinear meson coupling in NL models and by density dependence of the coupling constants, i.e., the density-dependent meson–nucleon vertices, in the DD-ME and DD-PC models.

Each of the classes in this paper is represented by CEDF models which are considered as the state of the art, i.e., by NL3*,[43] DD-ME2[44] and DD-PC1.[45] These parameters are briefly introduced below.

(i) NL3* is the modern, slightly improved version of the well-known NL3 functional. Both NL3 and NL3* functionals are based on the Walecka model[46] with their three mesons σ, ω and ρ and also include a density dependence through nonlinear meson couplings in the σ-channel. Both the functionals do not contain δ-meson. Besides the fixed values for the masses m, m_ω and m_ρ, there are six terms, i.e., m_σ, g_σ, g_ω, g_ρ and the nonlinear coupling terms g_2 and g_3, which fit well in Ref. 43 to a set of experimental data on spherical nuclei: 12 binding energies, nine charge radii and four neutron-skin thicknesses. NL3*, as all older nonlinear meson-coupling functionals like NL1,[47] NL3[33] or TM1,[48] has no nonlinearities in the isovector channel. There is an important difference between the functional NL3* and two other functionals, i.e., DD-ME2 and DD-PC1, namely NL3* has no nonlinearities in the

isovector channel and also in infinite nuclear matter, the isovector fields are proportional to the isovector density, which is given by $N - Z$.

(ii) In DD-ME models, the nucleus is described as a system of Dirac nucleons interacting via the exchange of mesons with finite masses, which leads to finite-range interactions. In DD-ME models there is no δ-meson. Here m, m_ω and m_ρ are fixed values. The density dependence of the coupling constants is given by four independent parameters. Along with the four independent parameters, i.e., m_σ, g_σ, g_ω and g_ρ, DD-ME2 contains eight independent parameters which have been fitted in Ref. 44 to a set of experimental data on spherical nuclei: 12 binding energies, nine charge radii and three neutron-skin thicknesses.

(iii) The Lagrangian in DD-PC1 contains the free-nucleon part, coupling of proton to the electromagnetic field and point-coupling interaction terms. The derivative term with the d'Alembert operator is for the effects of finite-range

Table 1. The parameters of the density functionals NL3*, DD-ME2 and DD-PC1. The masses are given in MeV, the parameter g_2 in NL3* is in fm^{-1} and all other parameters are dimensionless.

Parameter	NL3*[a]	DD-ME2[b]	DD-PC1[c]
m	939	939	939
m_σ	502.5742	550.1238	
m_ω	782.600	783.000	
m_ρ	763.000	763.000	
g_σ	10.0944	10.5396	
g_ω	12.8065	13.0189	
g_ρ	4.5748	3.6836	
g_2	−10.8093		
g_3	−30.1486		
a_σ		1.3881	
b_σ		1.0943	
c_σ		1.7057	
d_σ		0.4421	
e_σ		0.4421	
a_ω		1.3892	
b_ω		0.9240	
c_ω		1.4620	
d_ω		0.4775	
e_ω		0.4775	
a_ρ		0.5647	
a_s			−10.0462
b_s			−9.1504
c_s			−6.4273
d_s			1.3724
a_v			5.9195
b_v			8.8637
c_v			0.0
d_v			0.6584
$b_{\rm TV}$			1.8359
$d_{\rm TV}$			0.6403

[a] Ref. 43, [b] Ref. 44 and [c] Ref. 45.

interaction. Like the meson-exchange model, this model contains isoscalar–scalar (S), isoscalar–vector (V) and isovector–vector (TV) interactions. Ten density-dependent constant parameters in this model are a_s, b_s, c_s, d_s, a_v, b_v, c_v, d_v, b_{TV} and d_{TV}, which control the strength and density dependence of the interaction Lagrangian, that are adjusted using a multistep parameter in Ref. 45 fixed exclusively to the experimental masses of 64 axially deformed nuclei.

In the present work, the microscopic self-consistent RMF theory has been used as a standard tool to investigate the nuclear structure phenomena. The relativistic Lagrangian density (the modified original Walecka Lagrangian taking into account various limitations) for a nucleon–meson many-body system is explained by many authors in Refs. 26–29, 31, 32, 41, 49–53. The values of the parameters for NL3*, DD-ME2 and DD-PC1 are given in Table 1 as cited in Refs. 43–45, respectively. The numbers of independent parameters in NL3*, DD-ME2 and DD-PC1 are 6, 8 and 10, respectively.

2.1. *The β-decay half-life*

The β-decay half-life is determined in this paper by using the empirical formula given by Fiset and Nix.[54] The formula is mainly formulated for the superheavy mass region. The formula for β-decay half-life is defined as[54]

$$T_{\beta}^{1/2} = (540 \times 10^5)\frac{m_e^5}{\rho_{\mathrm{d.s.}}(W_{\beta}^6 - m_e^6)}. \tag{1}$$

The energy W_β is the total maximum energy of the emitted β-particle, including its rest mass m_e, i.e., $W_\beta = Q_\beta + m_e$. Here, $Q_\beta = \mathrm{BE}(Z+1, A) - \mathrm{BE}(Z, A)$. Beta decay or electron capture takes place only whenever Q_β or $Q_{\mathrm{e.c.}}$ is greater than zero. Below the line of β-stability $Q_{\mathrm{e.c.}}$ is negative, and above the line Q_β is negative.[54] Here, $\rho_{\mathrm{d.s.}}$ is the average density of states in the daughter nuclei and is equal to $e^{\frac{-A}{290}} \times$ number of states within 1 MeV of ground states. To find the value of $\rho_{\mathrm{d.s.}}$ the authors in Ref. 54 have used the empirical results given by Seeger *et al.*[55] For example, the values of $\rho_{\mathrm{d.s.}}$ are 2.73, 8.6 and 15.0 for even, odd-mass and odd nuclei, respectively, in deformed nuclei.[54]

It is difficult to evaluate the BE and quadrupole moment of odd-N or odd-Z or both odd-N and odd-Z (odd–even, even–odd or odd–odd) nuclei. To carry out this, we have to include extra time-odd term in the calculation. The time-reversal symmetry is violated in mean-field models for an odd–even or odd–odd nucleus. In RMF calculations, the space components of the vector fields are neglected, which are odd under time reversal and parity. These studies are useful in finding magnetic moments but have marginal effect on bulk properties such as BEs or quadrupole deformations[56] in the present context. In the odd-Z or odd-N calculations, we apply the Pauli blocking approximation,[37] which restores the time-reversal symmetry. In the above approach, one pair of conjugate states, $\pm m$, is removed from the pairing scheme. The odd particle exists in one of these states, and its corresponding conjugate state remains empty. In principle, we have to block different states around the

Fermi level in turn to find the one that gives the lowest energy configuration of the odd nucleus. For odd–odd nuclei, one needs to block both the odd neutron and the odd proton.[57]

2.2. *Total nuclear reaction cross-section*

The details of the calculation for the expression of total reaction cross-section (σ_R) using Glauber approach have been given by Glauber.[22,23] The standard Glauber form for the total reaction cross-section at high energies is expressed as[23,58,59]

$$\sigma_R = \int [1 - T(\mathbf{b})] d\mathbf{b}, \tag{2}$$

where $T(\mathbf{b})$ is the transparency function with impact parameter $\mathbf{b}$. The transparency function $T(\mathbf{b})$ can be expressed in terms of phase shift function as

$$T(\mathbf{b}) = \left| e^{\iota \chi_{\mathrm{PT}}(\mathbf{b})} \right|^2, \tag{3}$$

where χ_{PT} is the projectile–target phase shift function. This phase shift function is calculated by

$$\iota \chi_{\mathrm{PT}}(\mathbf{b}) = -\sum_{i,j} \sigma_{\mathrm{NN}} \int \overline{\rho_P}(\mathbf{s}) \overline{\rho_T}(|\mathbf{b} - \mathbf{s}|) d\mathbf{s}. \tag{4}$$

Here, the summation runs over nucleons i and j, where i belongs to projectile and j belongs to target nuclei. The subscripts P and T refer to projectile and target, respectively. σ_{NN} is the experimental nucleon–nucleon reaction cross-section which depends on the energy. The densities for projectile and target fit in Eq. (4) to fix the projectile–target phase shift function. The axially deformed densities cannot be used directly. For this, we have converted the deformed densities into spherical equivalent using two Gaussian functions[58]

$$\rho(r) = \sum_{i=1}^{2} c_i \exp[-a_i r^2]. \tag{5}$$

The z-integrated densities are defined as

$$\overline{\rho}(w) = \int_{-\infty}^{\infty} \rho\big(\sqrt{w^2 + z^2}\big) dz, \tag{6}$$

with $w^2 = x^2 + y^2$. Initially Glauber model was designed for the high-energy approximation. However, it was found to work reasonably well for both the nucleus–nucleus reaction and the differential elastic cross-sections over a broad energy range[58,60,61] by modified phase shift function as

$$\iota \chi_{\mathrm{PT}}(\mathbf{b}) = -\int_P \int_T \sum_{i,j} [\Gamma_{\mathrm{NN}}(b_{\mathrm{eff}}) \overline{\rho_P}(\mathbf{t}) \overline{\rho_T}(\mathbf{s})] d\mathbf{s} d\mathbf{t}, \tag{7}$$

where b_{eff}=$|\mathbf{b} - \mathbf{s} + \mathbf{t}|$, $\mathbf{b}$ is the impact parameter. Also $\mathbf{s}$ and $\mathbf{t}$ are the dummy variables for integration over the z-integrated target and projectile densities.

The projectile–target profile function $\Gamma_{\rm NN}$ for optical limit approximation is defined as

$$\Gamma_{\rm NN}(b_{\rm eff}) = \frac{1-\iota\alpha_{\rm NN}}{2\pi\beta_{\rm NN}^2}\sigma_{\rm NN}\exp\left(-\frac{b_{\rm eff}^2}{2\beta_{\rm NN}^2}\right) \tag{8}$$

for finite range, and

$$\Gamma_{\rm NN}(b_{\rm eff}) = \frac{1-\iota\alpha_{\rm NN}}{2}\sigma_{\rm NN}\delta(b_{\rm eff}) \tag{9}$$

for zero range.

The parameters $\sigma_{\rm NN}, \alpha_{\rm NN}$ and $\beta_{\rm NN}$ usually depend upon the proton–proton, neutron–neutron and proton–neutron interactions. Here $\sigma_{\rm NN}$ is the total nuclear reaction cross-section of NN collision, $\alpha_{\rm NN}$ is the ratio of the real part to the imaginary part of the forward nucleon–nucleon scattering amplitude and $\beta_{\rm NN}$ is the slope parameter. The slope parameter determines the fall of the angular distribution of the NN elastic scattering.

2.3. *Angular elastic differential cross-section*

The nucleus–nucleus elastic scattering amplitude is written as

$$F(\mathbf{q}) = \frac{\iota K}{2\pi}\int d\mathbf{b}e^{\iota\mathbf{q}\cdot\mathbf{b}}(1-e^{\iota\chi_{\rm PT}(\mathbf{b})}), \tag{10}$$

where K is the momentum of projectile and q is the momentum transferred from the projectile to the target. At low energy, this model is modified in order to take care of finite-range effects in the profile function and Coulomb-modified trajectories. The elastic scattering amplitude including the Coulomb interaction is expressed as

$$F(\mathbf{q}) = e^{\iota\chi_s}\left\{F_{\rm coul}(\mathbf{q}) + \frac{\iota K}{2\pi}\int d\mathbf{b}e^{\iota\mathbf{q}.\mathbf{b}+2\iota\eta\ln(Kb)}\left(1-e^{\iota\chi_{\rm PT}(\mathbf{b})}\right)\right\}, \tag{11}$$

with the Coulomb elastic scattering amplitude

$$F_{\rm coul}(\mathbf{q}) = \frac{-2\eta K}{q^2}\exp\left\{-2\iota\eta\ln\left(\frac{q}{2K}\right) + 2\iota{\rm arg}\Gamma(1+\iota\eta)\right\}. \tag{12}$$

Here $\eta = Z_P Z_T e^2/\hbar v$ is the Sommerfeld parameter, v is the incident velocity of the projectile and $\chi_s = -2\eta\ln(2Ka)$ with a being a screening radius. The elastic differential cross-section is given by[58,62]

$$\frac{d\sigma}{d\Omega} = |F(\mathbf{q})|^2. \tag{13}$$

Whereas the ratio of angular elastic differential cross-section to the Rutherford elastic differential cross-section is expressed as

$$\frac{d\sigma}{d\sigma_R} = \frac{\dfrac{d\sigma}{d\Omega}}{\dfrac{d\sigma_R}{d\Omega}} = \frac{|F(\mathbf{q})|^2}{|F_{\rm coul}(\mathbf{q})|^2}. \tag{14}$$

3. Results and Discussions

This section describes the numerical results for both even–even and even–odd nuclei of zirconium isotopic chain starting from ^{90}Zr to the expected drip-line nucleus ^{125}Zr. The ground state properties, i.e., binding energy, the RMS charge radius ($r_{\rm ch}$), quadrupole deformation parameter (β_2) and densities for Zr isotopic chain, are being estimated within the RMF approximation using NL3*, DD-ME2, DD-PC1 parameter sets with spherical and deformed nuclei. However, the study of bulk properties of these nuclei is carried out merely to show the applicability of the formalism near drip-line. The calculated results are presented below through various figures along with the experimental data, wherever available, and are explained briefly.

3.1. *Density distributions*

The nucleonic density distribution in our case is the sum of neutron and proton densities along z-axis, i.e.,

$$\rho(r_\perp, z) = \rho_p(r_\perp, z) + \rho_n(r_\perp, z). \tag{15}$$

We have shown the radial density plots, by taking the RMF spherical densities of projectiles for some key isotopes of Zr up to drip-line nuclei in Figs. 1 and 2. In Fig. 1, the radial density plots for ^{90,98,100,102}Zr and in Fig. 2 the same for ^{104,112,122,125}Zr isotopes are given. Here the nucleonic density distributions contain larger values at the center and the values keep on decreasing as the radius increases. The small depletion in densities appears at the center for ^{90,98,100,102,104}Zr isotopes, which is the primary indication for their bubble structure. It also appears from the

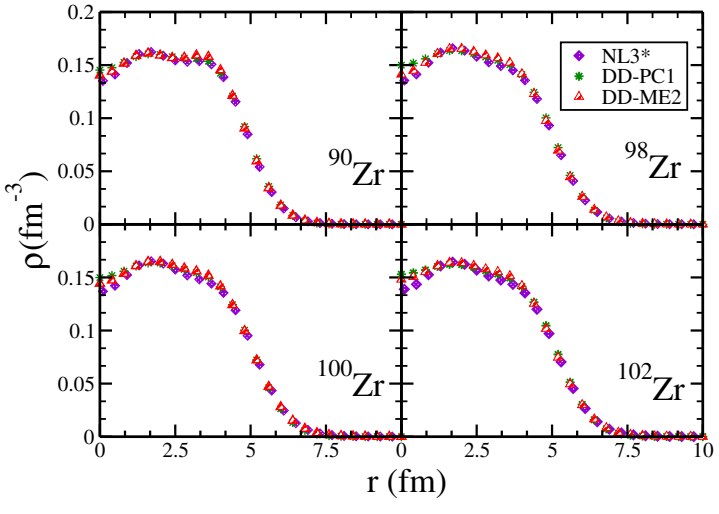

Fig. 1. Radial density plots for ^{90,98,100,102}Zr obtained from RMF (NL3*), DD-ME2 and DD-PC1 parameters for spherical densities.

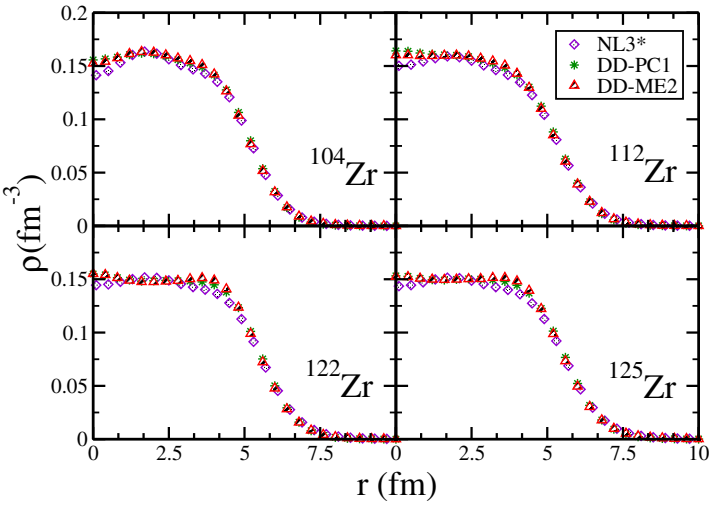

Fig. 2. Same as Fig. 1 but for ^{104,112,122,125}Zr isotopes.

figures that densities of the considered set of nuclei show a similar kind of trend for all the parameter sets. One may also observe from the figure that the skin effect increases with increase of isotopic mass number. These densities can be fed as an input to the Glauber model after converting them into spherical equivalent in terms of Gaussian coefficients.

3.2. *Binding energy*

Binding energy indicates the stability of nuclei as well as α-or β-decay energies. Here, the binding energies for all the isotopic chains of zirconium, starting from ^{90}Zr to drip-line nucleus ^{125}Zr, are presented in Fig. 3. Deeply observing the results, it is found that ^{90}Zr remains in prolate deformation in intrinsic excited state. While moving from mass number $A = 91$ to $A = \pm 97$, a shape transition occurs from prolate to oblate. The zirconium isotopes are known to possess, a rapidly changing nuclear shape when the neutron number changes from 56 to 60, i.e., $A = 96 - 100$.[65] It may be the reason for the transition from oblate to prolate shape from ^{98}Zr to ^{101}Zr and hence further, transition from prolate to oblate shape of the nuclei occurring between ^{102}Zr and ^{112}Zr. In Ref. 66, the authors have predicted about the structure of the nuclei, with the results obtained by using the self-consistent HFB mean-field theory, that a spherical ground state shape is preferred over a prolate shape starting from the ^{114}Zr isotope up to the drip-line nucleus. We found the prolate deformation to be dominant over oblate deformation from ^{113}Zr isotope to the expected drip-line nucleus ^{125}Zr. From the overall observation of all the considered isotopes, it is found that the results obtained for binding energy of the isotopes of zirconium, i.e., $^{90-125}$Zr, underestimate both the FRDM[63] and experimental data.[64]

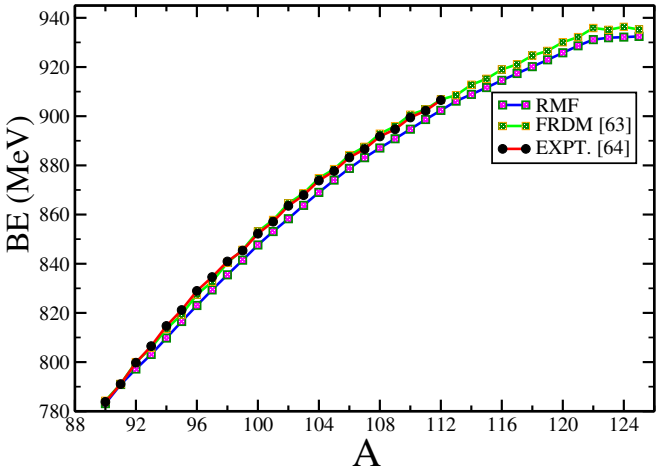

Fig. 3. The variations of binding energy of isotopes of zirconium from ^{90}Zr to the drip-line nucleus ^{125}Zr with respect to mass number A. The FRDM results are taken from Ref. 63 and the experimental data are taken from Ref. 64.

3.3. *Charge radius*

The root-mean-square charge radius ($r_{\rm ch}$) is obtained by taking into account the finite size of the proton using simple mathematical relation: $\langle r_{\rm ch}\rangle = \sqrt{\langle r_p^2\rangle + 0.64}$. Here, the constant factor 0.64 represents the finite size effects of protons with radius 0.8 fm. Figure 4(a) represents the charge radii of the considered isotopic chain of

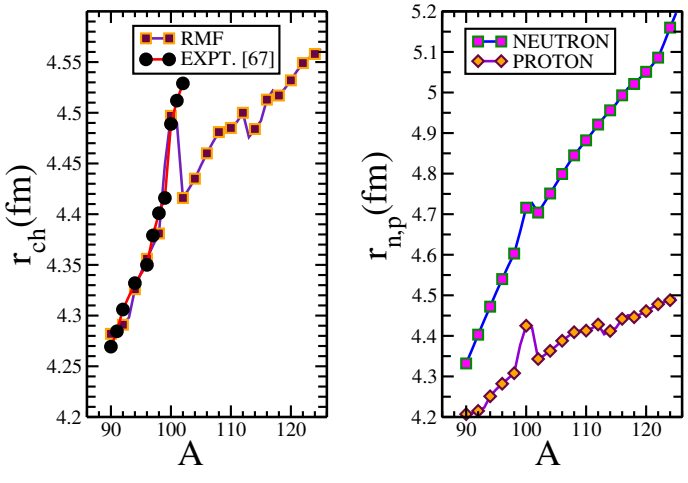

(a) (b)

Fig. 4. (a) Variation of charge radius ($r_{\rm ch}$) obtained from RMF (NL3*) parameter set with respect to mass number, along with the experimental data[67] given for comparison. (b) Variations of neutron and proton radii estimated from RMF formalism with respect to mass number.

zirconium estimated from RMF (NL3*) formalism along with the available experimental data.[67] One can notice that the obtained results show nice agreement with the experimental data for lighter isotopes, i.e., up to $N = 61$, then a fall in the charge radii occurs at $N = 62, 72, 78$, which signals the transition from prolate to oblate or vice versa, as also explained in Ref. 16. As these charge radii are obtained from the density profiles and are consistent with the experimental data,[67] undoubtedly we can use these density profiles to study the β-decay half-life and the nuclear reaction cross-section. In Fig. 4(b) the root-mean-square neutron and proton radii predicted from RMF (NL3*) formalism are plotted against mass number for zirconium isotopic chain. In the figure, there is a gradual increase in neutron and proton radii with the increase of mass number and the results for neutron radius overestimate those of the proton radius.

To be more clear about the structure of these nuclei, skin thicknesses $(r_n - r_p)$ of these nuclei obtained from NL3*, DD-ME2 and DD-PC1 parameter sets are plotted against isospin asymmetric $I = (N - Z)/A$ along with the experimental data taken from Ref. 68, in Fig. 5. Here the results for Δr_{np} $(= r_n - r_p)$ obtained from NL3* overestimate the experimental data, whereas the results from DD-ME2 and DD-PC1 are in agreement with the data. The reason for the overestimation of $r_n - r_p$ is due to the absence of $\omega - \rho$ cross-coupling and the large value of asymmetry coefficient for this set.[69] Also in Ref. 70, authors have mentioned that NL3* gives larger values of skin thickness for NL models due to the absence of nonlinearities in the isovector channels.

It is worthy to mention here that although the density-dependent parameter sets DD-ME2 and DD-PC1 reproduce the neutron-skin thicknesses of Zr isotopes

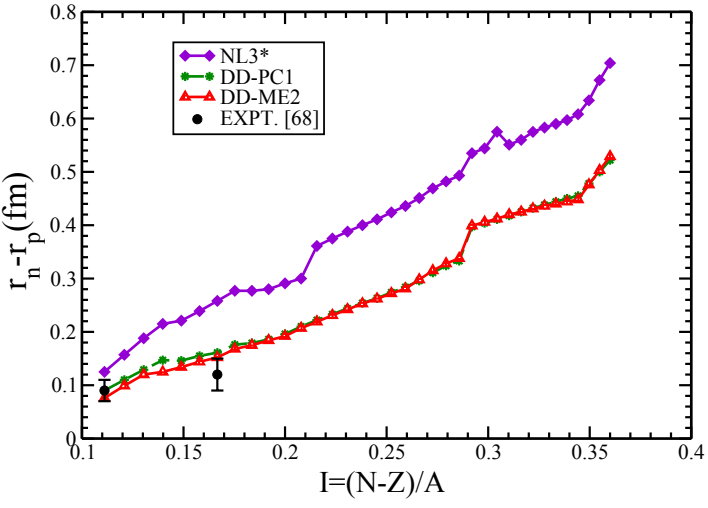

Fig. 5. The variations of difference between neutron and proton RMS radii, i.e., $\Delta r_{np} (= r_n - r_p)$ obtained from NL3*, DD-ME2 and DD-PC1 parameter sets as a function of isospin asymmetric $I = (N - Z)/A$. The experimental data displayed are taken from Ref. 68.

quite well with the experimental values for two isotopes ^{90,96}Zr, it is not clear so far about the uncertainty in the measurement of the neutron distribution radius.[71] To take care of the uncertainty in the measurement of r_n, the experiments at JLab[72] are proposed. Thus, it is too early to say the exact value of the neutron distribution radius for nuclei like Zr isotopes. On the other hand NL3 parameter set[33] is widely used in the literature, which reproduces the experimental binding energy, charge distribution radius and quadrupole moments nicely throughout the periodic table. The present NL3* set[43] is an improved version of NL3 and may be more suitable to use for finite nuclei.

3.4. *Quadrupole deformation*

The total quadrupole deformation parameter β_2 is obtained from the summation of the individual proton and neutron quadrupole moments, as[30]

$$Q = Q_p + Q_n = \sqrt{\frac{16\pi}{5}} \left(\frac{3}{4\pi} AR^2 \beta_2 \right). \tag{16}$$

The results of quadrupole deformation parameter for the whole isotopic chain of zirconium from NL3* parameter set are compared with the data[73] as shown in Fig. 6. The obtained results of β_2 in our calculation for ^{102}Zr and ^{104}Zr are 0.43 and 0.423, respectively, which are very close to the experimental values[73] i.e. 0.43 for ^{102}Zr and 0.38 for ^{104}Zr. We have also found very large prolate deformation for $^{102–112}$Zr nuclei and the spherical ground state shape for $^{113–123}$Zr.

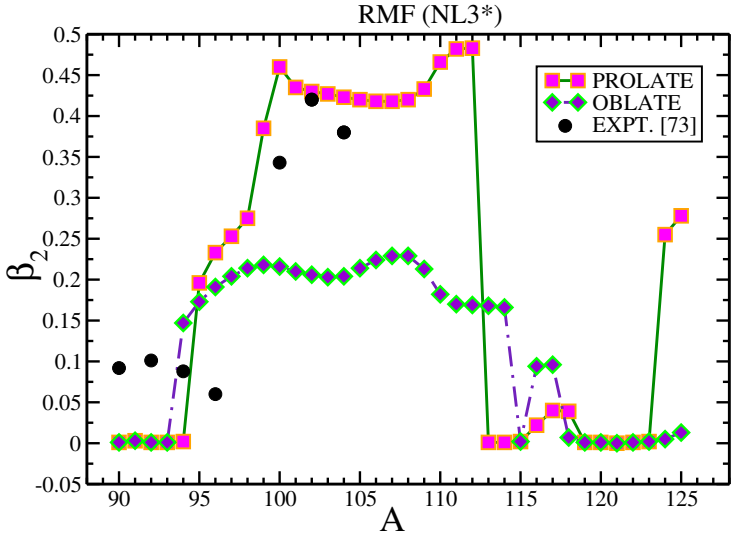

Fig. 6. Variation of quadrupole deformation parameter β_2 obtained from RMF (NL3*) parameter set with respect to mass number, along with available experimental data.[73]

3.5. *Neutron separation energy*

The one/two-neutron separation energy $[S_n(N,Z)/S_{2n}(N,Z)]$ can be estimated from the ground state nuclear binding energies of BE(N,Z), BE$(N-1,\ Z)$ and BE$(N-2,\ Z)$ with the relations:

$$S_n(N,Z) = \mathrm{BE}(N,Z) - \mathrm{BE}(N-1,Z) \tag{17}$$

and

$$S_{2n}(N,Z) = \mathrm{BE}(N,Z) - \mathrm{BE}(N-2,Z). \tag{18}$$

The BEs of ${}^{A}X_Z$ and ${}^{A-2}X_Z$ are calculated from RMF (NL3*) formalism. It is essential to have very precise mass measurements to predict the correct estimations of the neutron separation energies S_n and S_{2n}. In β-decay one neutron is transformed into a proton, an electron and an anti-neutrino. The position of the two-neutron drip-line is defined by the condition $S_{2n}(N,Z) = 0$, and nuclei with negative two-neutron separation energy are unstable against the emission of two neutrons. In Fig. 7, we display the calculated S_{2n} values for ${}^{90-125}$Zr from RMF (NL3*) formalism along with the FRDM[63] results and experimental data,[64] for both even and odd nuclei separately. From the figure, we notice that S_{2n} values agree well with FRDM calculations for both even and odd nuclei. Evidently, the S_{2n} decreases gradually with the increase in mass number except for some noticeable kinks at $A = 95, 96, 121, 122$ and drops to a value approaching zero at $A = 125$, showing the expected drip-line of zirconium isotopic chain.

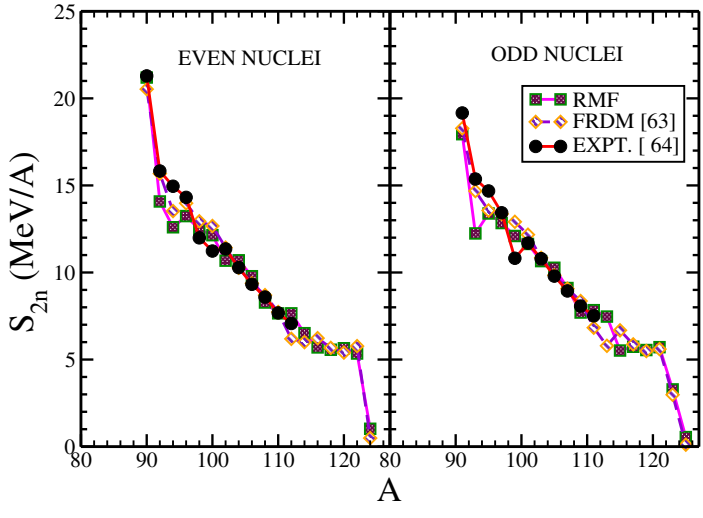

Fig. 7. The variations of difference of two-neutron separation energies of ${}^{90-125}$Zr with respect to mass number, compared with FRDM[63] and experimental data.[64]

3.6. *The Q-value and β-decay half-life*

The neutron-rich nuclei like zirconium favorably exhibit β-decay above α-decay.[74] The β-decay half-life values of zirconium isotopes have been determined in this paper by using the empirical formula given by Fiset and Nix.[54] Though the formula is mainly formulated for the superheavy mass region, but in this work we have checked its credibility in intermediate mass region too. Recently, an experiment was carried out to measure the mass of the ^{104}Zr isotope[65] and triple-γ coincidence experiments are also carried out with the Gammasphere at LBNL, in order to determine the half-lives and quadrupole deformations of the neutron-rich ^{102,104}Zr isotopes. The isotopes in this region are produced in the process of fission of transuranic elements and have been studied via γ-ray spectroscopy techniques.[76] These medium-mass nuclei are among the most neutron-rich isotopes ($N/Z \approx 1.6$) for which spectroscopic data are available. In Fig. 8, we have compared the β-decay energies of the Zr isotopes up to the drip-line obtained using RMF (NL3*) formalism with FRDM[75] and experimental data[73] with the variation of mass number A. It can be seen that the β-decay energy increases with the increase of neutron number and the results are also consistent with the data[73] except for ^{94}Zr. The β-decay half-lives of $^{90-125}$Zr isotopes have been estimated by using the empirical formula given by Fiset and Nix in Ref. 54 with RMF (NL3*) densities and given are in Table 2. The decay of these nuclei usually follows β-decay as the prominent path due to the neutron richness. Closely observing the results, it is found that the results are not fairly matching with the data up to ^{102}Zr but from ^{103}Zr onwards till the expected drip-line the estimated results follow a similar trend as FRDM[75] and also with the experimental data[73] up to ^{112}Zr.

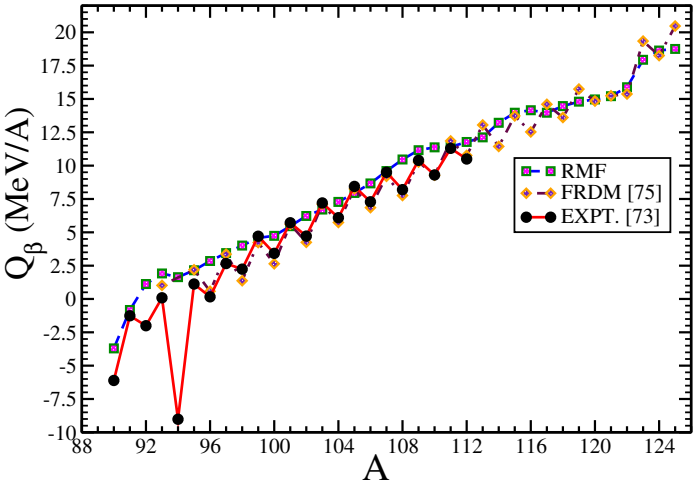

Fig. 8. The variation of β-decay energy (Q_β) (in MeV), obtained from RMF (NL3*) parameter set, with respect to mass number A for the isotopic chain of zirconium, compared with FRDM[75] and experimental data.[73]

Table 2. The β-decay energy Q_β (in MeV/A) and half-life T_β from RMF (NL3*) formalism are compared with the FRDM predictions[75] and the experimental data.[73]

	Q_β(MeV/A)			T_β		
Nucleus	RMF	FRDM[75]	EXPT.[73]	RMF	FRDM[75]	EXPT.[73]
^{90}Zr	−3.706		−6.111	883.69 s		809.2 ms
^{91}Zr	−0.825		−1.258	−0.563 y		
^{92}Zr	1.122		−2.006	13.87 h		
^{93}Zr	1.915	1.02	0.090	0.41 h	>100	1.61×10^6 y
^{94}Zr	1.636		−9.017	2.7 h		
^{95}Zr	2.155	2.19	1.123	845.531 s	>100	64.032 d
^{96}Zr	2.847	0.58	0.162	669.304 s	>100	2.35×10^{19} y
^{97}Zr	3.443	3.36	2.66	79.992 s	>100	16.749 h
^{98}Zr	4.006	1.37	2.238	113.76*s*	>100	30.7 s
^{99}Zr	4.581	4.23	4.707	17.66 s	>100	2.1 s
^{100}Zr	4.737	2.64	3.421	46.57 s	102.16 s	7.1 s
^{101}Zr	5.459	5.60	5.717	6.8 s	53.712 s	2.3 s
^{102}Zr	6.226	4.25	4.717	10.48 s	9.8 s	2.9 s
^{103}Zr	6.708	7.11	7.204	2.2 s	1.95 s	1.32 s
^{104}Zr	7.279	5.74	6.095	4.4 s	1.88 s	0.87 s
^{105}Zr	7.95	8.26	8.441	0.856 s	0.102 s	0.66 s
^{106}Zr	8.668	6.85	7.29	1.66 s	0.381 s	0.191 s
^{107}Zr	9.593	9.20	9.5	0.297 s	0.223 s	0.138 s
^{108}Zr	10.462	7.76	8.2	0.57 s	0.18 s	0.073 s
^{109}Zr	11.159	10.27	10.4	0.126 s	0.142 s	0.063 s
^{110}Zr	11.371	9.28	9.3	0.358 s	0.081 s	0.037 s
^{111}Zr	11.404	11.85	11.3	0.112 s	0.063 s	>392 ns
^{112}Zr	11.775	10.77	10.5	0.295*s*	0.046 s	>394 ns
^{113}Zr	12.122	13.05		0.079 s	0.036 s	
^{114}Zr	13.214	11.44		0.153 s	0.02 s	
^{115}Zr	13.967	13.73		0.035 s	0.017 s	
^{116}Zr	14.156	12.53		0.103 s	0.0124 s	
^{117}Zr	13.968	14.6		0.035 s	0.0123 s	
^{118}Zr	14.467	13.61		0.092 s	0.0094 s	
^{119}Zr	14.797	15.74		0.026 s	0.0086 s	
^{120}Zr	14.964	14.84		0.076 s	0.0069 s	
^{121}Zr	15.209	15.24		0.022 s	0.011 s	
^{122}Zr	15.882	15.37		0.054 s	0.0043 s	
^{123}Zr	17.938	19.34		0.0085 s	0.0108 s	
^{124}Zr	18.634	18.25		0.0215 s	0.0043 s	
^{125}Zr	18.752	20.47		0.0066 s	0.0038 s	

It is to be noted here that in the present calculation we have followed the Pauli blocking procedure.[37,57] As a result, the odd–even staggering in binding energy is observed for even and odd nuclei but Q_β is obtained from the same mass number A of the two nuclei which differ by one unit of proton and neutron, respectively. In one case we should block the odd-neutron and in other case the odd-proton. Thus, the difference in Q_β values arising from the neutron or proton blocking contribution in the binding energy should reflect in the results of Q_β. But the present blocking scheme is not sufficient to reflect the effect as it is experimentally seen. Our results show that β-decay half-life has higher value for nuclei having a lower

neutron number from the whole isotopic chain. These new results will encourage experimentalists to proceed further in Zr isotopes study.

3.7. *Reaction and differential cross-section*

In the measurement of reaction parameters through Glauber formalism, the essential ingredients for evaluation of profile function are both its energy as well as isospin-dependent parameters. The values of these parameters at $E_{\mathrm{Proj}} = 30\,\mathrm{MeV/nucleon}$ and $425\,\mathrm{MeV/nucleon}$ are $\sigma_{\mathrm{NN}} = 19.6\,\mathrm{fm}^2$ and $3.025\,\mathrm{fm}^2$, $\alpha_{\mathrm{NN}} = 0.87$ and 0.36 and $\beta_{\mathrm{NN}} = 1.0\,\mathrm{fm}^2$ and $0.48\,\mathrm{fm}^2$, respectively, as estimated from Ref. 77.

We have presented in Figs. 9 and 10 the calculated results for the reaction cross-section σ_R obtained from NL3*, DD-ME2 and DD-PC1 parameter sets for both spherical and deformed densities of the projectile nuclei ^{90,98,100,102,104,112,122,125}Zr and target nucleus ^{12}C. If we go deep into the figures, it could be seen that σ_R of the nuclei sharply decreases with increase of the projectile energy up to 50 MeV/A, then it increases rapidly for increase of incident energy up to 100 MeV/A, subsequently it decreases up to 300 MeV/A and remains almost constant thereafter throughout the range of projectile energy. The fact behind the sharp decrease of reaction cross-section at higher energy may be due to the inappropriate maintenance of geometrical limit, i.e., at these energies some transparency occurs in nucleon–nucleus interaction. Again there is a rapid decrease in σ_R with increasing energy up to 300 MeV/A at which point π production causes the cross-section to rise. This remarkable dip in cross-section can be traced to be due

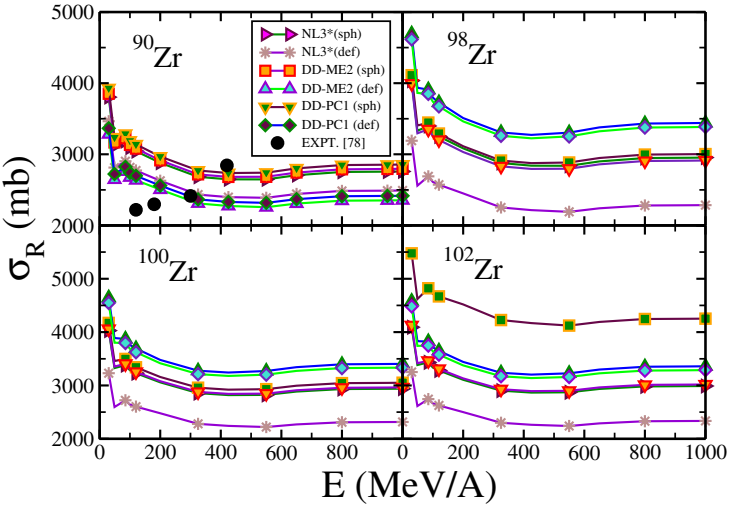

Fig. 9. The Coulomb-modified reaction cross-section σ_R variations (in mb) of ^{90,98,100,102}Zr reacting with ^{12}C at projectile energy in 1 GeV/A range, obtained from NL3*, DD-ME2 and DD-PC1 parameter sets along with the available experimental data.[78]

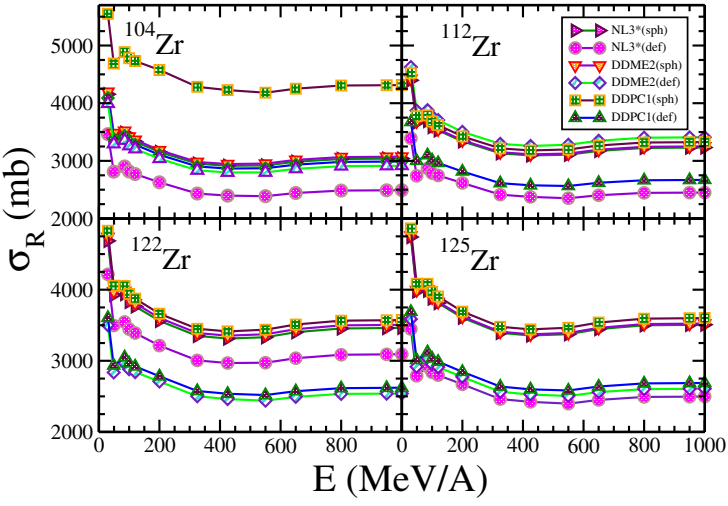

Fig. 10. Same as Fig. 9 but for projectiles ^{104,112,122,125}Zr.

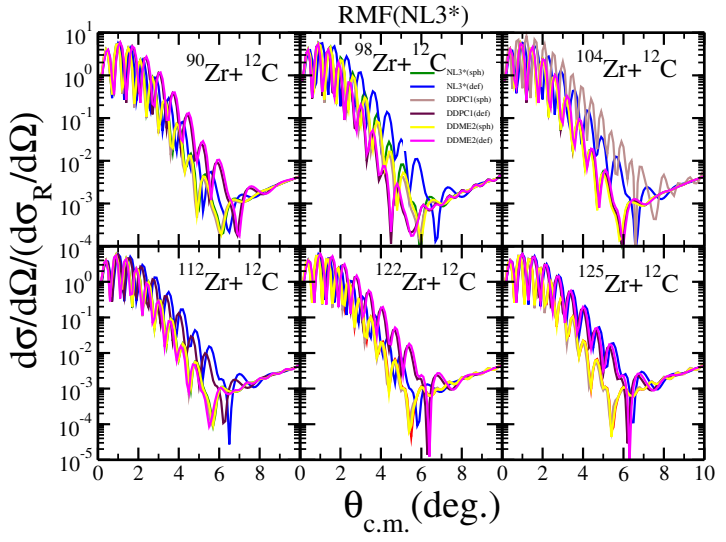

Fig. 11. Differential elastic scatterings for ^{90,98,104,112,122,125}Zr $+^{12}$ C reactions at relativistic projectile energy of 800 MeV/nucleon as a function of scattering angle using NL3*, DD-ME2 and DD-PC1 deformed densities.

to the behavior of the scattering phase shift. The dip should be a characteristic feature of any heavier system which is dominated by the nucleon–nucleon interaction.[79]

Due to the insufficiency in the reaction cross-section data for the nucleus–nucleus system we are unable to find the actual reason behind the abrupt changes in it. In

Ref. 79, it is assumed that, due to the strong absorption of composite projectiles and heavy ions, at low energy, σ_R simply levels off, above the Coulomb barrier, at geometrical limit and remains constant with that value at intermediate and higher energies. Very few experimental data are available in this energy range of projectile. Hence in Fig. 9, we have compared our results with the available experimental data[78] for ^{90}Zr as projectile and ^{12}C as target. It is found that, at the projectile energies of 420 MeV/A (in case of spherical nuclei) and 300 MeV/A (in case of deformed nuclei), our predicted value of σ_R is closer to the available experimental data.[78] To get more precise knowledge of the applicability of the results, we need the data for more energy range too.

To explain the scattering phenomena, the study of differential cross-section is required. Figure 11 shows our results obtained from NL3*, DD-ME2 and DD-PC1 parameter sets for ^{90,98,104,112,122,125}Zr as projectiles and ^{12}C as target at a projectile energy of 800 MeV/A. We found that the diffraction dissociation decreases with increasing scattering angles and disappears at higher angles for all cases of the nuclei taken into consideration.

4. Conclusions

In summary, the bulk properties like binding energy, RMS charge radius and quadrupole deformation parameter for various isotopes of zirconium up to the drip-line region are studied using RMF (NL3*, DD-ME2 and DD-PC1) formalism. These results agreed reasonably with FRDM model as well as with experimental data. The one- and two-proton/neutron separation energies of these isotopes are also explained. The Q_β values and the β-decay half-lives of neutron-rich $^{90–125}$Zr are discussed. The β-decay energy and the β-decay half-life of these neutron-rich isotopes have been calculated to know the stability of these isotopes. It is observed from our calculated results that β-decay half-life has a higher value for nuclei having a lower neutron number. The finite life of some zirconium isotopes could be suitable for nuclear reactors. The predicted results of half-life for $^{113–125}$Zr isotopes will encourage experimentalists to study these isotopes. The total nuclear cross-sections for ^{90,98,100,102,104,112,122,125}Zr as projectiles and ^{12}C as target have been calculated in the Glauber Model using RMF densities for projectile energy range of 30–1000 MeV and we observed similar trend for all parameter sets taking both spherical and deformed densities into consideration. The elastic differential cross-sections are also studied for some of the key isotopes in the isotopic chain. These cross-section data in a broad energy range will provide a better understanding of the properties of zirconium.

Acknowledgments

This work is supported by the Department of Science and Technology, Govt. of India, Project No. EMR/2015/002517.

References

1. K. Heyde, P. Van Isacker, M. Waroquier, J. L. Wood and R. A. Meyer, *Phys. Rep.* **102** (1983) 291.
2. J. L. Wood, K. Heyde, W. Nazarewicz, M. Huyse and P. Van Duppen, *Phys. Rep.* **215** (1992) 101.
3. T. Kibedi, G. D. Dracoulis, A. P. Byrne, P. M. Davidson and S. Kuyucak, *Nucl. Phys. A* **567** (1994) 183.
4. P. M. Davidson, G. D. Dracoulis, T. Kibedi, A. P. Byrne, S. S. Andersssen, A. M. Baxter, B. Fabricius, G. J. Lane and A. E. Stuchbery, *Nucl. Phys. A* **568** (1994) 90.
5. L. Bianco *et al.*, *Phys. Lett. B* **690** (2010) 15.
6. J. Kurcewicz *et al.*, *Phys. Lett. B* **717** (2012) 371.
7. K. Heyde and J. L. Wood, *Rev. Mod. Phys.* **83** (2011) 1467.
8. H. Watanabe *et al.*, *Phys. Rev. Lett.* **111** (2013) 152501.
9. J. Meng and P. Ring, *Phys. Rev. Lett.* **80** (1998) 460.
10. M. G. Mayer, *Phys. Rev.* **75** (1949) 1969.
11. J. Blons, *Nucl. Phys. A* **502** (1989) 121.
12. T. Sumikama *et al.*, *Phys. Rev. Lett.* **106** (2011) 202501.
13. J. Dobaczewski, N. Michel, W. Nazarewicz, M. Ploszajczak and M. V. Stoitsov, in *A New Era of Nuclear Structure Physics*, eds. Y. Suzuki, S. Ohya, M. Matsuo and T. Ohtsubo (World Scientific, Singapore, 2004), pp. 162–171.
14. J. Meng and S. G. Zhou, *J. Phys. G* **42** (2015) 093101.
15. K. Nomura, R. Rodriguez-Guzman and L. M. Robledo, *Phys. Rev. C* **94** (2016) 044314.
16. M. Bhuyan, *Phys. Rev. C* **92** (2015) 034323.
17. B. Kumar, S. K. Singh and S. K. Patra, *Int. J. Mod. Phys. E* **24** (2014) 1550017.
18. J. Enders, H. Kaiser, P. von Neumann-Cosel, C. Rangacharyulu and A. Richter, *Phys. Rev. C* **59** (1999) R 1851(R).
19. P. M. Prajapati *et al.*, *Nucl. Sci. Eng.* **171** (2012) 78.
20. A. B. Smith *et al.*, Nuclear data and measurement series: An evaluated neutronic data file for elemental zirconium Technical Report No. ANL/NDM-134, Argonne National Laboratory, JL, USA (1994).
21. P. Campbell *et al.*, *Phys. Rev. Lett.* **89** (2002) 082501.
22. R. J. Glauber, *Phys. Rev.* **100** (1955) 24.
23. R. J. Glauber, in *High Energy Collision Theory*, eds. W. E. Brittin and L. C. Dunham, Lectures on Theoretical Physics, Vol. 1 (Interscience, New York, 1959), p. 315.
24. M. Bhuyan, S. K. Patra, P. Arumugam and R. K. Gupta, *Int. J. Mod. Phys. E* **20** (2011) 1227.
25. M. Bender, P.-H. Heenen and P.-G. Reinhard, *Rev. Mod. Phys.* **75** (2003) 121.
26. P. G. Reinhard, *Rep. Prog. Phys.* **52** (1989) 439.
27. N. Paar, D. Vretenar and G. Colo, *Rep. Prog. Phys.* **70** (2007) 691.
28. D. Vretenar, A. V. Afanasjev, G. A. Lalazissis and P. Ring, *Phys. Rep.* **409** (2005) 101.
29. J. Meng, H. Toki, S. G. Zhou, S. Q. Zhang, W. H. Long and L. S. Geng, *Prog. Part. Nucl. Phys.* **57** (2006) 470.
30. S. K. Patra and C. R. Praharaj, *Phys. Rev. C* **44** (1991) 2552.
31. B. D. Serot and J. D. Walecka, *Adv. Nucl. Phys.* **16** (1986) 1.
32. P. Ring, *Prog. Part. Nucl. Phys.* **37** (1996) 193.
33. G. A. Lalazissis, J. Konig and P. Ring, *Phys. Rev. C* **55** (1997) 540.
34. M. M. Sharma, M. A. Nagarajan and P. Ring, *Phys. Lett. B* **312** (1993) 377.

35. R. J. Furnstahl, B. D. Serot and H. B. Tang, *Nucl. Phys. A* **615** (1997) 441.
36. M. Del Estal, M. Centelles, X. Viñas and S. K. Patra, *Phys. Rev. C* **63** (2001) 044321.
37. S. K. Patra, M. Del Estal, M. Centelles and X. Viñas, *Phys. Rev. C* **63** (2001) 024311.
38. B. D. Serot and J. D. Walecka, *Int. J. Mod. Phys. E* **6** (1997) 515.
39. A. Shukla, B. K. Sharma, R. Chandra, P. Arumugam and S. K. Patra, *Phys. Rev. C* **76** (2007) 034601.
40. B. K. Sharma, S. K. Patra, R. K. Gupta, A. Shukla, P. Arumugam, P. D. Stevenson and G. Walter, *J. Phys. G* **32** (2006) 2089.
41. S. K. Patra, R. N. Panda, P. Arumugam and R. K. Gupta, *Phys. Rev. C* **80** (2009) 064602.
42. R. N. Panda and S. K. Patra, *Int. J. Mod. Phys. E* **20** (2011) 2505.
43. G. A. Lalazissis, S. Karatzikos, R. Fossion, D. Pena Arteaga, A. V. Afanasjev and P. Ring, *Phys. Lett. B* **36** (2009) 671.
44. G. A. Lalazissis, T. Niksic, D. Vretenar and P. Ring, *Phys. Rev. C* **71** (2005) 024312.
45. T. Niksic, D. Vretenar and P. Ring, *Phys. Rev. C* **78** (2008) 034318.
46. J. D. Walecka, *Ann. Phys.* (*New York*) **83** (1974) 491.
47. P.-G. Reinhard, M. Rufa, J. Maruhn, W. Greiner and J. Friedrich, *Z. Phys. A* **323** (1986) 13.
48. Y. Sugahara and H. Toki, *Nucl. Phys. A* **579** (1994) 557.
49. W. Pannert, P. Ring and J. Boguta, *Phys. Rev. Lett.* **59** (1987) 2420.
50. G. A. Lalazissis, S. Raman and P. Ring, *At. Data Nucl. Data Tables* **71** (1999) 1.
51. M. Bhuyan, S. K. Patra and R. K. Gupta, *Phys. Rev. C* **84** (2011) 014317.
52. T. Niksic, D. Vretenar and P. Ring, *Prog. Part. Nucl. Phys.* **66** (2011) 519.
53. S. K. Patra and C. R. Praharaj, *Phys. Lett. B* **273** (1991) 13.
54. E. O. Fiset and J. R. Nix, *Nucl. Phys. A* **193** (1972) 647.
55. P. A. Seeger, W. A. Fowler and D. D. Clayton, *Astrophys. J. Suppl.* **11** (1965) 121.
56. G. A. Lalazissis, D. Vretenar and P. Ring, *Nucl. Phys. A* **650** (1999) 133.
57. B. Kumar, S. K. Biswal, S. K. Singh and S. K. Patra, *Phys. Rev. C* **92** (2015) 054314.
58. B. Abu-Ibrahim, Y. Ogawa, Y. Suzuki and I. Tanihata, *Comput. Phys. Commun.* **151** (2003) 369.
59. P. J. Karol, *Phys. Rev. C* **11** (1975) 1203.
60. J. Chauvin, D. Lubrun, A. Lounis and M. Buenerd, *Phys. Rev. C* **28** (1983) 1970.
61. M. Buenerd, A. Lounis, J. Chauvin, D. Lebrun, P. Martin, G. Duhamel, J. C. Gondrand and P. D. Saintignon, *Nucl. Phys. A* **424** (1984) 313.
62. M. K. Sharma, R. N. Panda, M. K. Sharma and S. K. Patra, *Phys. Rev. C* **93** (2016) 014322.
63. P. Moller, A. J. Sierk, T. Ichikawa and H. Sagawa, *At. Data Nucl. Data Tables* **109–110** (2016) 1.
64. M. Wang *et al.*, *Chin. Phys. C* **36** (2012) 1603.
65. S. Rinta-Antila, S. Kopecky, V. S. Kolhinen, J. Hakala, J. Huikari, A. Jokinen, A. Nieminen, J. Äystö and J. Szerypo, *Phys. Rev. C* **70** (2004) 011301(R).
66. A. Blazkiewicz, V. E. Oberacker and A. S. Umar, *Phys. Rev. C* **71** (2005) 054321.
67. I. Angeli and K. P. Marinova, *At. Data Nucl. Data Tables* **99** (2013) 69.
68. J. Jastrzebski *et al.*, *Int. J. Mod. Phys. E* **13** (2004) 343.
69. B. G. Todd-Rutel and J. Piekarewicz, *Phys. Rev. Lett.* **95** (2005) 122501.
70. S. E. Agbemava *et al.*, *Phys. Rev. C* **95** (2017) 054324.
71. B. A. Brown, *Phys. Rev. Lett.* **85** (2000) 5296.
72. R. Michaels, P. A. Souder and G. M. Urciuoli, Update of E00003: Neutron skin of ^{208}Pb through parity violating electron scattering, Jefferson Lab PAC 23, Jefferson Lab, Newport News (2003).

73. National Nuclear Data Center, NuDat 207: Based on ENSDF and the Nuclear Wallet Cards, Brookhven National Laboratory, Upton, USA (2016).
74. S. Mahapatra, C. Lahiri, B. Kumar, R. N. Mishra and S. K. Patra, *Int. J. Mod. Phys. E* **25** (2016) 1650062.
75. P. Moller, J. R. Nix and K. L. Kratz, *At. Data Nucl. Data Tables* **66** (1997) 131.
76. J. K. Hwang, A. V. Ramayya, J. H. Hamilton, D. Fong, C. J. Beyer, P. M. Gore, E. F. Jones, Y. X. Luo, J. O. Rasmussen, S. J. Zhu, S. C. Wu, I. Y. Lee, P. Fallon, M. A. Stoyer, S. J. Asztalos, T. N. Ginter, J. D. Cole, G. M. Ter-Akopian and R. Donangelo, *Phys. Rev. C* **69** (2004) 057301.
77. W. Horiuchi, Y. Suzuki, B. Abu Ibrahim and A. Kohama, *Phys. Rev. C* **75** (2007) 44607.
78. C. C. Sahm *et al.*, *Phys. Rev. C* **34** (1986) 2165.
79. R. M. DeVries and J. C. Peng, *Phys. Rev. C* **22** (1980) 1055.